Nanostructured metal-N-C electrocatalysts for CO_2 reduction and hydrogen evolution reactions

Aaron Roy[a], Dorottya Hursán[b,c], Kateryna Artyushkova[a], Plamen Atanassov[a], Csaba Janáky[b,c,**], Alexey Serov[a,*]

[a] Department of Chemical and Biological Engineering, Center Micro-Engineered Materials (CMEM), MSC01 1120 University of New Mexico Albuquerque, NM, 87131, USA
[b] Department of Physical Chemistry and Materials Science, University of Szeged, Aradi sq. 1, 6720, Szeged, Hungary
[c] MTA-SZTE "Lendület" Photoelectrochemistry Research Group, Szeged, Rerrich sq. 1, 6720, Hungary

ARTICLE INFO

ABSTRACT

Major efforts are devoted to find efficient and selective electrocatalysts for solar fuel generation, thus enabling accelerated development of such technologies. A series of electrocatalysts from the metal–nitrogen–carbon (M–N–C) family was synthesized by a sacrificial support method (SSM). The salts of Cu, Mo, Pr, and Ce were employed as metal-precursors while the N–C network was formed by the high temperature pyrolysis of aminoantipyrine (AAPyr) organic compound. The structural and chemical features of the obtained electrocatalysts were characterized by SEM, XRD, TEM, BET, and XPS methods. Electrochemical characterization was performed towards CO_2 electroreduction (CO_2ER) and Hydrogen Evolution Reactions (HER) in neutral media. The metal-free N-doped carbon had a notable activity towards CO_2ER, with the predominant formation of carbon monoxide (CO). This was also confirmed by isotopic labeling experiments, to exclude the possible contribution of the electrocatalyst as a carbon source. Upon introducing the metals into the carbon structure, the electrocatalytic activity towards HER increased. Particularly impressive current densities were achieved for the Cu and Mo-containing electrodes, where the presence of metal–N bonds was identified. These structural motifs are likely to be the electrocatalytic centers in the structure for the HER, which will be further studied for other metal-containing nanocarbons in our laboratories.

1. Introduction

Electrochemical water-splitting and electroreduction of carbon dioxide to form useful chemicals attract the attention of many research groups around the world [1]. The increase of interest is mainly related to the substantial improvement in efficiency of harvesting the different renewable energy sources, such as wind, solar and tidal, which can be coupled with CO_2 or water electrolyzers. The electrochemical conversion of carbon dioxide can be a beneficial tool for decreasing the amount of a greenhouse gas and also to generate useful products for the chemical industry [2]. It was shown previously that products of CO_2-reduction could be varied in a broad range, spanning through carbon monoxide, formic acid, hydrocarbons (e.g., methane and ethylene) as well as alcohols (methanol, ethanol, isopropyl alcohol, etc.) [3,4]. In his pioneering study, Hori performed a comparative analysis of the electrocatalytic activity of different metal surfaces in CO_2ER towards the production of chemicals mentioned above and established fundamental structure–property relationships [3]. The main focus of CO_2ER research has remained the same during the past two decades, targeting the design of metallic and alloyed electrocatalysts [5]. Other electrode materials, such as oxides, chalcogenides, and carbides were also studied in CO_2ER [5–7].

Research on carbon-based electrocatalysts has gained an increasing momentum in both HER [8] and CO_2ER [9]. These studies focused on achieving both higher efficiency/selectivity as well as on understanding the underlying fundamental principles. It was soon realized that heteroatom-doping of the carbon structure can result in the formation of electrocatalytically active sites towards HER or CO_2ER. Usually nitrogen acts as the primary dopant while S, P, or B atoms are the secondary dopant elements [10]. In this vein, a graphitic carbon nitride/N-doped graphene catalyst showed notable HER activity with good stability both in acidic and alkaline medium [11]. In another study on N- and S co-doped nanoporous graphene, it was found that coupling of electronic structures of S and N dopants with their geometric effects is

---

responsible for the HER performance [12]. Nitrogen and P co-doped 3D graphitic carbon materials showed excellent catalytic activity both in HER and ORR [8,12]. A systematic investigation was carried out on N,B- N,P-, and N,S- co-doped carbon catalysts to study the effect of the secondary dopant atoms. The introduction of S atoms had the greatest promoting effect in the HER activity, followed by the P atoms, while co-doping with B, reduced the activity of the catalytic activity compared to the bare N-doped catalyst [13].

There are also examples for the CO$_2$ER on N-doped carbon electrodes. For example, in the case of N-doped CNTs, CO was formed as the reduction product with the maximum Faradaic efficiency of 80% at E = −0.78 V (vs. RHE). Based on the experimental data as well as density functional theory and computational hydrogen model calculations, it was found that the N-atoms have a crucial role in CO$_2$-reduction, the most efficient N configuration being the pyridinic N followed by pyrrolic and graphitic N [14]. In another study, 3D graphene foam was modified with graphitic-C$_3$N$_4$. The FE for CO-formation reached 85% with −1.8 mA cm^{-2} total current density at −0.58 V (vs. RHE). HCOO$^-$ was also formed at this potential with 3% FE. The catalyst with the highest pyridinic N-content showed the highest performance towards CO formation; however, the contribution of other types of nitrogen atoms was not ruled out [15]. Nitrogen-doped, carbon-coated MWCNTs were tested in a microfluidic CO$_2$ electrolysis cell where the catalyst layer was uniformly coated on a gas diffusion electrode. The cell produced a partial CO current density of up to 90 mA cm^{-2} at −1.62 V (vs. Ag/AgCl). The FE for CO formation was around 98%, outperforming the state-of-the-art Ag nanoparticle catalyst [16]. A series of nitrogen-doped CNTs with tailored nitrogen contents and fractions of pyrrolic, pyridinic, and quaternary nitrogen species was synthesized via the adjustment of the amount of nitrogen source and calcination temperature. Based on DFT calculations and the Tafel analysis, the most active site is quaternary nitrogen, followed by the pyridinic and pyrrolic nitrogen [17]. In another study, the onset potential of CO formation showed a positive correlation with the pyridinic and graphitic nitrogen contents, but the catalytic activity of pyridinic or graphitic nitrogen site alone couldn't be distinguished [18]. A study on N-doped graphene-like materials indicated that the active N species play a crucial role in the high selectivity of CH$_4$ [19]. The CO$_2$-reduction activity of N-doped graphene quantum dots was compared to that of N-doped, reduced graphene oxide. This latter one primarily facilitated CO formation, while hydrocarbons were only detected at more negative potentials compared to quantum dots. This suggested that the morphology also plays a key role in the CO$_2$-reduction activity. Specifically, the pyridinic N at the edge site was suggested to be more active to induce C–bond formation than those at the basal plane [20]. The effect of pore size was studied for other carbons as well, including some S-containing dopant [21]. Highly porous N- and S- co-doped carbon gel was produced from porous organic polymer precursors and used in the CO$_2$ER. CO and trace amounts of CH$_4$ were formed as reduction products [22]. Recently, part of this team performed isotope labeling studies to furnish mechanistic insights into the electrochemical CO$_2$ reduction on N-doped carbon electrodes. By using non-equilibrated solutions of the selectively labeled the initial carbon sources (i.e., ^{13}CO$_2$ and H^{13}CO$_3^-$), bicarbonate anion was identified as the predominant source of the carbon monoxide reduction product [23].

One of the newest classes of electrode materials for HER and CO$_2$ER is based on transition metal–nitrogen–carbon frameworks (M–N–Cs); rooted in the use of these materials in the oxygen-reduction reaction (ORR) [6,7,24–26]. By analogy with ORR catalysts, the transition metal in these studies usually was Fe, Co, or Ni. For example, a Ni–C catalyst, containing atomically isolated Ni species anchored on graphitized carbon exhibited outstanding performance towards HER [27]. In another study, Co–C–N catalysts were synthesized from in situ electrochemically polymerized polyaniline and Co-ion precursors, by carbonization at different temperatures (550 °C–950 °C) [28]. Even bimetallic catalysts were studied, where HER was driven on a Mo–Ni–N–C system

[29]. As for CO$_2$ER, these M–N–C catalysts are also becoming more and more popular. Commercial carbon blacks were first functionalized with nitrogen and Fe and/or Mn ions using high temperature pyrolysis and acid leaching. The catalysts were active to form CO/H$_2$ mixtures outperforming a low-area polycrystalline gold benchmark [30]. In another study, the formation of CO with high Faradaic efficiency was demonstrated on a Fe–N–C catalyst, and the selectivity of these materials for CO$_2$ER over HER depended on the ratio of isolated FeN$_4$ sites vs. Fe-based nanoparticles [26]. Ni–N–Gr samples exhibited high activity for CO formation, and the atomic Ni coordinated with N in the graphene network was identified as active reaction center [31]. Another Ni–N–C catalyst exhibited over 90% Faradaic efficiency towards CO formation with current density as high as 28.6 mA cm^{-2}. The high catalytic activity was attributed to the abundant Ni-N$_4$ active sites [32]. Most recently, M–N–C catalysts with different metal atoms (Mn, Fe, Co, Ni, Cu, Cr) [33,34] were studied, where Fe and Ni were identified as the most active metals, especially in the M-N$_x$ configuration. Single atomic Ni catalysts, where Ni is embedded in a carbon matrix are gaining special interest in the electrochemical CO$_2$ reduction [35,36].

Herein, we report the first study on M–N–C catalysts with M = Cu, Mo, Ce, and Pr (as well as the bare C–N material with no metal added) towards CO$_2$ER and HER. We have shown that the highest CO selectivity in the series was observed for the bare carbon–nitrogen catalyst, while the addition of the metals from the group mentioned above shifted the selectivity toward the production of hydrogen while boosting the total current density. Overall, the Cu and Mo-containing carbon nanostructures behaved like a very promising electrocatalyst in HER, operating in neutral media.

2. Experimental

2.1. M–N–C catalysts synthesis

The materials synthesis was performed by a sacrificial support method (SSM) using Cu, Mo, Pr and Ce as metals, and aminoantipyrine as a source of nitrogen and carbon [37–40]. In general, after dissolving 10 g of aminoantipyrine in water, 5 g of sacrificial support LM 150 silica (a surface area ~150 m^2 g^{-1}) was added. The amount of N–C precursor, as well as the metal salt, was calculated to be 25 wt% on silica after pyrolysis. The metal salts were: nitrates in the case of Cu, Pr and Ce, while ammonium heptamolybdate was used as a source of Mo (all chemicals were purchased from Sigma-Aldrich). The amounts of metal salts added to AAPyr + SiO$_2$ mixture were: 1.5 g of copper nitrate, 1.75 g of praseodymium nitrate, 1.6 g of cerium nitrate and 0.75 g of ammonium heptamolybdate. After mixing the metal salts, N–C precursor and silica, water was evaporated at 85 °C for 8 h s. The dried mixture was grounded using a mortar and pestle then pyrolyzed at T = 945 °C for 45 min in a N$_2$ stream flowing at 100 ccm, the ramp rate was fixed as 10 °C/deg. Silica was dissolved in 40 wt% HF for 24 h, and the black residual powder was washed with deionized water until neutral pH was reached (~pH = 6.56). After drying the powder on air at T = 85 °C, for 8 h, a second heat treatment was carried out in 10% NH$_3$ atmosphere at 945 °C for 15 min, ammonia flow rate was 100 ccm, ramp rate was 25 deg/min. The bare N–C catalyst was synthesized by the same method with no metal salt added.

2.2. Physical characterization

Powdered samples were analyzed by X-ray diffraction (XRD) using a Rigaku SmartLab diffractometer (Bragg-Brentano geometry), D-tex Ultra silicon strip detector, and a Cu K$_\alpha$ X-ray source (1.54 Å) operating at 40 kV and 40 mA. Whole pattern refinement was performed with MDI JADE software (from MDI, Inc.). Scanning Electron Microscopy (SEM) was performed using a Hitachi S-5200 Nano SEM with 15 keV accelerating voltage. Transmission electron microscopy (TEM) was performed using a JEOL 2010 instrument with 200 keV accelerating

voltage. XPS spectra were acquired on a Kratos Axis Ultra DLD X-ray photoelectron spectrometer using a monochromatic Al Kα source operating at 150 W with no charge compensation.

2.3. Electrochemical measurements

The catalyst samples were spray-coated on a glassy carbon (GC) substrate, which was manually polished and thoroughly rinsed with ethanol, acetone, and water for 5 min before spray-coating. A homogenous suspension, containing 50 mg catalyst, 5 cm^3 ethanol (96%, VWR), 5 cm^3 deionized water, and 250 µl Nafion dispersion (10 wt%, FuelCell Store) was prepared by sonication, in an ultrasonic bath for 1 h (Elmasonic P70H, 37 Hz at 220 W). The spray-coating was performed with a custom-designed, automated spray-coater, where the GC was heated to 110 °C. The exact catalyst loading was always determined by weighing the glassy carbon-supported catalyst layers. After careful optimization (see Fig. 5), layers with 1.5 mg cm^{-2} loading were prepared for the electrocatalytic measurements, unless otherwise stated.

Electrochemical measurements were performed in a classical three-electrode cell using an AUTOLAB PGSTAT204 potentiostat/galvanostat. The working electrode was the glassy-carbon supported catalyst layer, with 1 cm^2 and 2 cm^2 geometrical surface areas for the electrochemical characterization (cyclic voltammetry, linear sweep voltammetry) and the potentiostatic electrolysis (and product detection), respectively. The current densities were always normalized by the geometrical electrode surface areas. The reference electrode was a Ag /AgCl/3 M NaCl electrode, while the counter electrode was a Pt foil. All potentials were measured versus the Ag/AgCl/3 M NaCl reference electrode and converted to the reversible hydrogen electrode (RHE) scale using the following equation: $E_{(RHE)} = E_{(Ag/AgCl)} + 0.059 \, pH + E°_{(Ag/AgCl)}$. The anode and cathode compartments of the cell was separated by a Nafion-117 ion exchange membrane, to avoid any unwanted product cross-over.

Before electrocatalytic measurements, the catalyst layers were potentiodynamically cycled in the supporting electrolyte (at 200 mV s^{-1} sweep rate) between $E = -1.0$ and -0.4 V until the shapes of the consequent voltammograms were identical. The upper potential limit was chosen to avoid the oxidation and incidental dissolution of the metals from the carbon structure. CO$_2$ electroreduction experiments were performed in a 0.5 M KHCO$_3$ solution saturated with CO$_2$ before the measurements (pH = 7.4). Linear sweep voltammograms (LSVs) were recorded between $E = -0.4$ and -1.5 V, at 5 mV s^{-1} sweep rate. Blank measurements were performed (i.e., without CO$_2$) in a 0.5 M phosphate buffer saturated with N$_2$, having nearly the same pH (7.2) as the CO$_2$ saturated 0.5 M KHCO$_3$. The relative electrochemically active surface area of the catalysts was estimated from the charge capacitance of the catalyst layers, compared to the bare glassy carbon (1 cm^2 geometrical surface area and assuming surface roughness of 1). These double layer capacitance values were determined from the cyclic voltammograms (CVs) (0.5 M KHCO$_3$ / CO$_2$; 50 mV s^{-1} sweep rate, between -0.8 and -0.45 V). Finally, the charge capacitances measured for the catalyst layers were divided by the charge capacitance of a 1 cm^2 smooth glassy carbon electrode, thus obtaining the relative roughness.

CO$_2$-reduction products in the gas phase were analyzed with a Shimadzu GC-2010 Plus gas chromatograph equipped with a barrier discharge ionization detector (BID). A HP-PLOT Molisieve column was used for the separation. Samples from the gas phase were taken at 10, 30, and 50 min s and injected into the GC with an on-line sampling system. Oven program: 40 °C (6 min) -30 °C min^{-1} $- 200$ °C (4 min), injection temperature: 250 °C, linear velocity, 45.6 cm s^{-1}, split ratio: 40. The liquid-phase products were analyzed with a Shimadzu GC–MS QP 2010 S gas chromatograph–mass spectrometer (column: ZB-FFAP) after removing the electrolyte ions with an Amberlite IRN-150 ion exchange resin. Liquid samples were taken a few seconds after the gas samples. Oven program: 40 °C (3.5 min) $-$ 50 °C min^{-1} $-$ 70 °C -10 °C min^{-1} 170 °C $-$ 50 °C/ min $-$ 250 °C (5 min), injection

temperature: 200 °C, linear velocity: 40 cm s^{-1}, split ratio: 10.

Isotopic labeling experiments were performed using 0.1 M NaH^{13}CO$_3$ (98% ^{13}C, Sigma-Aldrich) electrolyte saturated with ^{12}CO$_2$ gas. First, the electrolysis cell was filled with 35 cm^3 ultrapure water and bubbled with ^{12}CO$_2$ for 30 minute s. Then the appropriate amount of NaH^{13}CO$_3$ was added to the ^{12}CO$_2$-saturated water, and the cell was immediately sealed. Before starting the electrolysis, the electrolyte was stirred for two hours to reach the isotope equilibrium between the gas phase CO$_2$ and the aqueous bicarbonate. Having 35 cm^3 electrolyte and 29 cm^3 headspace volume in the cathode compartment of our electrolysis cell, the ratio of the total ^{13}C to the total ^{12}C was 1.5 in equilibrium (25 °C, atmospheric pressure). This ratio was validated by GC–MS analysis, which was employed to monitor the equilibration process. During the electrolysis, 100 µl of the headspace gas was injected to a Shimadzu 2010 GC–MS equipped with an RT®-Molsieve 5 A column with a gas-tight syringe. Oven program: 35 °C (2 min) → (10 °C/min) → 150 °C (5 min), injection temperature: 200 °C, split ratio: 50:1, pressure control mode (50 kPa).

3. Results and discussion

The phase analysis of all crystalline materials present in the catalysts was performed by X-ray diffraction (Fig. 1). For the Cu, Pr, and Ce-containing samples, the dominant crystalline phase was the respective fluoride, where hexagonal PrF$_3$ and CrF$_3$ were phase pure. The hexagonal Cu$_7$(OH)$_{10}$F$_4$ was identified as the dominant phase of the Cu–N–C catalyst, with minor phases of cubic CuO, cubic Cu$_2$O, and cubic Cu, respectively (all phases are all known to be active in CO$_2$ER [41]). Unlike Cu-, Ce-, and Pr-derived materials, there were no crystalline phases observed in the Mo–N–C catalyst. Since molybdenum fluorides and molybdenum oxy-fluorides are soluble in water and would have been washed out during the etching procedure, the lack of crystalline material in this sample indicated that the Mo domains are not sufficient in size to produce coherent scattering at a detectable level. Importantly, beyond the detected crystalline phases, SSM also results in an atomically dispersed metal atom in the carbon structure [42]. Such metal content has an important impact on the overall electrocatalytic performance as shown below.

To monitor the metal dispersion on the support, the morphology of M–N–C catalysts was studied by both scanning- and transmission electron microscopy (Fig. 2). As expected from the XRD results, Ce–N–C, Cu–N–C, and Pr–N–C catalysts had nanoparticles
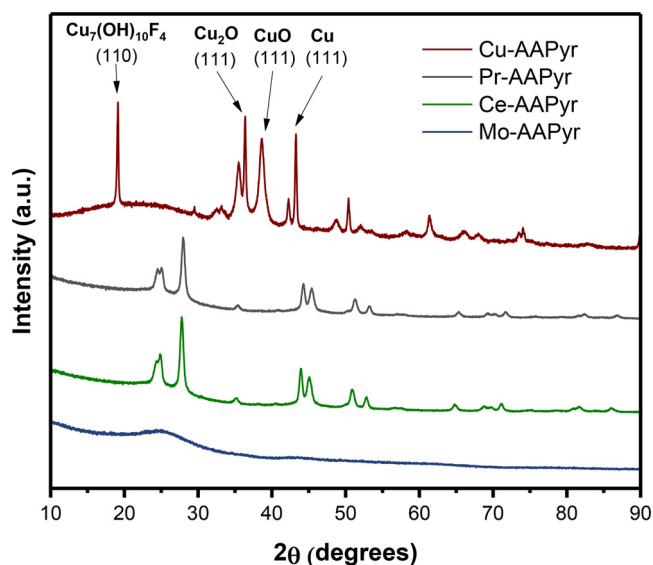

Fig. 1. XRD patterns for M–N–C catalysts where M = Cu, Pr, Ce, and Mo. Dominant reflections for various phases in the Cu–N–C catalyst are indicated.
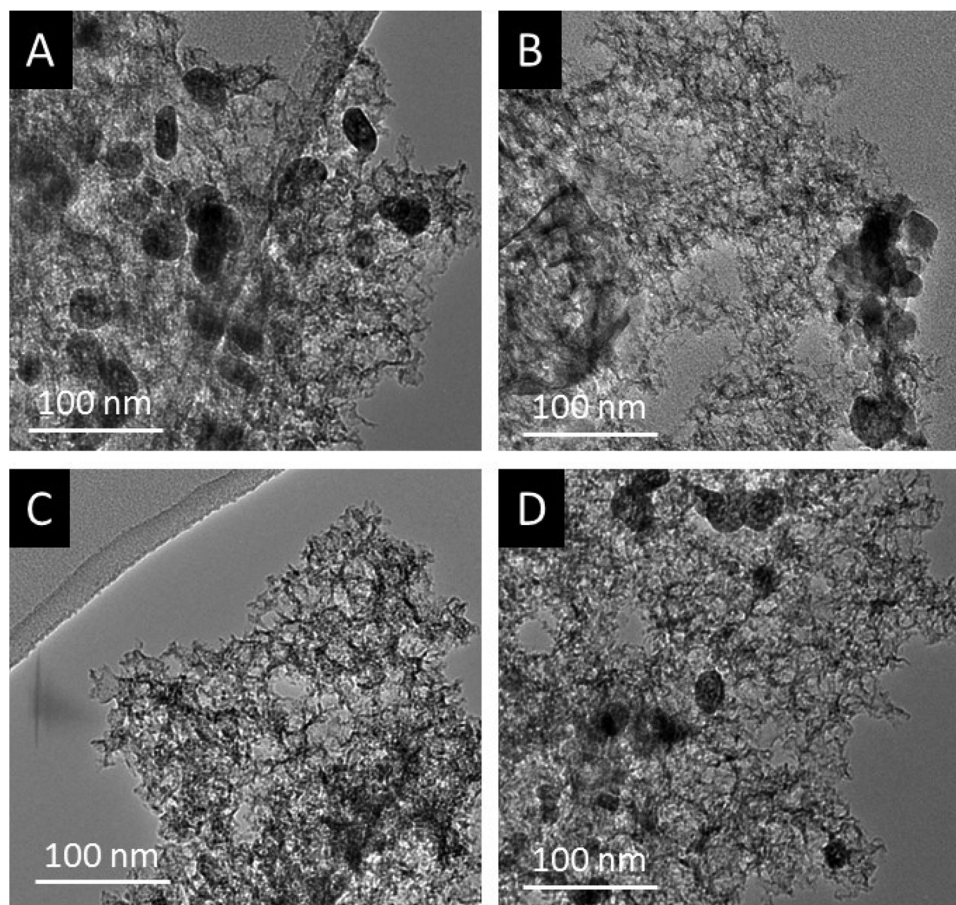
Fig. 2. TEM images recorded for the M–N–C electrocatalysts, where M is Ce (A), Cu (B), Mo (C), and Pr (D).

approximately 20–50 nm in size, as well as particles on the order of several nanometers. For Mo–N–C, we only observed small particles (a few nanometers in diameter) dispersed throughout the sample without signs of agglomeration. Given the domain sizes for crystalline materials calculated by XRD pattern refinement (15 nm – 67 nm), the composition of the smaller (< 5 nm) particles cannot be identified as oxides or fluorides. Though the smaller sized particles are found in all M–N–C catalysts, they are most abundant in Cu–N–C and Mo–N–C, where the latter consists entirely of such particles.

A typical SEM image is shown in Fig. 3 for the Cu–N–C catalyst. The overall morphology is very similar to those observed previously for other M–N–C materials obtained via the SSM method [43,44]. The
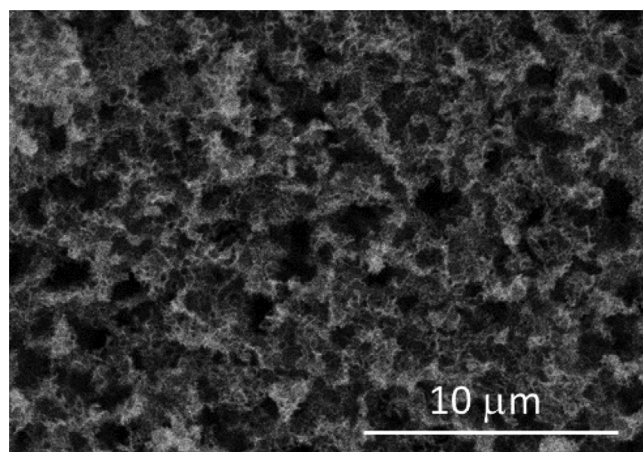

Fig. 3. SEM image of a Cu–N–C electrocatalyst.

highly porous nature of materials can be explained by two factors: the removal of silica particles and the decomposition of organic precursor molecules. Previously we controlled and optimized the pore modality and pore size distribution by selection of different types of silica particles [45]. In the present work ~50–70 nm silica particles were employed, to have an open-frame structure with a high density of active sites.

Surface chemical analysis of the materials was carried out by XPS. The overall elemental composition and quantitative relative nitrogen speciation is summarized in Table 1. Between 3 and 6 atomic percent of nitrogen was detected in all catalysts. Interestingly, the bare C–N sample had the lowest N-content, which suggests that the presence of the metal precursor during the synthesis changes the pyrolysis conditions as well. The identified nitrogen species are typical for such M–N–C materials [46], with the largest contribution coming from pyridinic and hydrogenated N atoms. The metal-free sample had the largest relative amount of hydrogenated nitrogen and smallest pyridinic nitrogen peak. Mo and Cu-containing samples had the largest amount of pyridinic nitrogen and the smallest amount of protonated and oxidized nitrogen (see the example of Cu–N–C in Fig. 4A). The Pr-based sample, in addition to having the smallest nitrogen and metal incorporated into the matrix, also had the largest amount of hydrogenated nitrogen. Ce–N–C had the smallest amount of pyridinic nitrogen and largest amount of oxidized and protonated nitrogen atoms.

The Cu-, and Mo–N–C samples had relatively higher amounts of metals (~3 at%), while Pr–N–C had only minor traces of Pr. Evaluating the metal type is also important for deriving structure-to-property correlations (see discussion below). Ce showed metallic Ce and oxides present, while Pr was mainly present in its oxide phase. Cu had a strong metallic peak, while Cu coordinated to nitrogen, and Cu-oxides were

Table 1
The surface composition of the various electrocatalyst samples, as deduced from XPS analysis.

	C %	O %	N %	M %	N pyridinic %	N_x-M/ N amine %	N hydrogenated %	N_{gr} + N^+ %	N^+/NO %
Mo-C-N	84.2	7.7	4.9	3.2	42	9	27	17	5
Ce-C-N	83.2	10.4	5.4	1.0	15	16	24	12	33
Pr-C-N	85.5	10.9	3.4	0.2	27	16	33	9	15
Cu-C-N	77.3	14.0	5.8	3.0	31	19	26	10	14
C-N	93.9	3.6	2.6	0.0	15	11	30	21	23

also detected. Finally, the Mo-based material had mainly oxide present, together with a minor portion of Mo coordinated to nitrogen.

Before studying the CO_2ER and HER properties of the carbon catalysts, cyclic voltammograms (CVs) were recorded in a potential window where no faradaic reaction takes place (Fig. 4A). From the CV scans the actual surface area of the catalysts were estimated. Strikingly higher currents were recorded for all carbon catalysts, compared to the bare glassy carbon electrode used for benchmarking purposes. Moreover, their electrical conductivity seems to be sufficiently high, as only little distortion from the perfect rectangular shape was seen in the CVs. Double layer capacitances were calculated from the CVs and compared to that of the bare GC. Assuming that the GC has a totally smooth surface (i.e., the surface roughness of 1), the ratio between the charge capacitances of the carbon catalysts and the GC gives a rough estimate of the electrochemically active surface areas of the catalysts (see Table 2 for the quantitative comparison). The presence of different metals during the synthesis seems to have a notable effect in the case of the Mo–N–C and Ce–N–C, as they have the significantly higher surface area, compared to the Pr-, and Cu- containing, as well as the metal-free carbon. The surface area of the Pr–N–C and the Cu–N–C was, however, were only slightly higher compared to the metal-free N–C catalyst.

The electrocatalyst film thickness was systematically optimized, by varying the M–N–C catalyst loading between 0.5 – 2.0 mg cm^{-2}. The highest currents were measured at 1.5 mg cm^{-2}, so this loading was chosen for all further studies. The electrochemically active surface areas of the catalyst layers with the identical optimized loading were compared to the bare glassy carbon electrodes. These values were calculated from the double-layer capacitances values, determined from the CVs (Fig. 5). Also note the good reproducibility of the electrode preparation, as the electrodes with similar weight have very similar electrochemical properties.

Linear sweep voltammograms (LSV curves) were recorded in a CO_2-saturated 0.5 M $KHCO_3$ electrolyte to evaluate the CO_2ER and HER properties of the catalyst samples (Fig. 6B). The behavior of the Pr–N–C and the N–C was almost identical, while there was a slight current increase below $E = -0.7$ V (vs. RHE) for the Ce-containing sample. In contrast, the Mo-, and Cu-containing catalysts show about 300 mV less negative onset potential and considerably higher reduction currents, compared to the metal-free catalyst. Interestingly, there is no direct correlation between the electrochemical surface area and the electrocatalytic performance: the higher reduction currents are not the
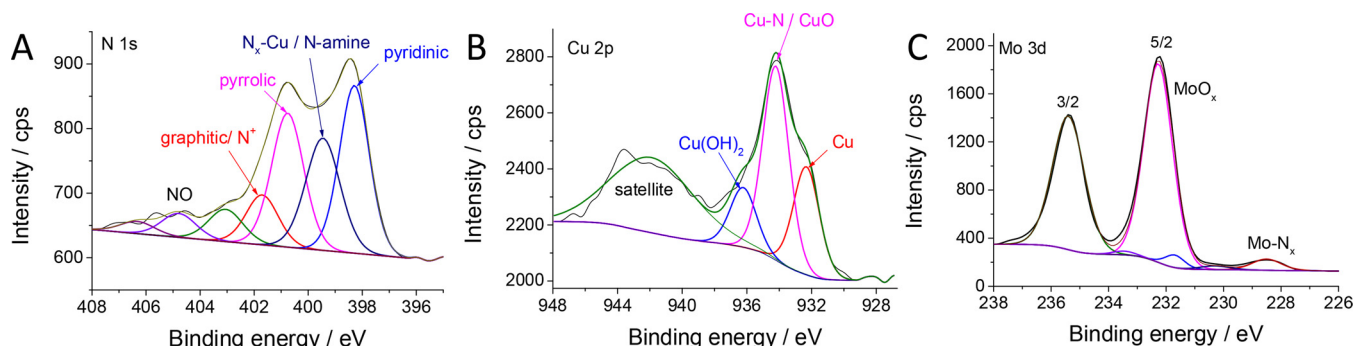
Table 2
Relative electrochemically active surface area of the M–N–C catalysts.

Catalyst	Electrochemically active surface area / 1 cm² geometric area
Mo–N–C	302
Ce–N–C	291
Pr–N–C	190
Cu–N–C	170
N–C	145

consequence of the higher surface area (see the example of Cu–N–C). This trend indicates that differences in the chemical structure have a major influence on the electrocatalytic behavior, which dominates over simple geometric effects. Additional comparative measurements were carried out with GC and Cu-foil electrodes as benchmarks (Fig. 6C), and impressively higher currents were detected for the Cu–N–C catalyst. Even more importantly, the more positive onset potential (see the inset of Fig. 6C), compared to the Cu foil, indicated that the current enhancement is not simply rooted in a surface area effect (i.e., the presence of nanoparticulate Cu vs. Cu foil), but in other, chemical underpinnings.

As the reduction currents in the presence of CO_2 is attributed to the superposition of the HER and CO_2ER, we performed control measurements (without CO_2) to differentiate between these two processes. The LSV curves are shown for the example of Cu–N–C (Fig. 6D). The overall shape of the voltammograms is very similar in the presence and the absence of CO_2. A slightly (about 100 mV) less negative onset potential and higher reduction current densities were observed in CO_2 for both samples, suggesting that CO_2 reduction takes place in parallel with H_2 evolution.

Long-term potentiostatic electrolysis was performed at three different potentials to test the stability of the catalysts and to analyze the products formed during the reduction. The chronoamperometric curves for all electrocatalysts are presented in Fig. 7. The stationary reduction current densities follow the trend which was observed during the LSV experiments. The Cu–N–C appeared to be less stable at more negative potentials than the other four samples, most probably because of the partial leaching of the larger sized nanoparticles. For the Ce- and Mo–N–C, however, there was practically no current decrease after the stationary current was reached (about 180 s). This suggests that in addition to the catalytic performance, the stability is also strongly

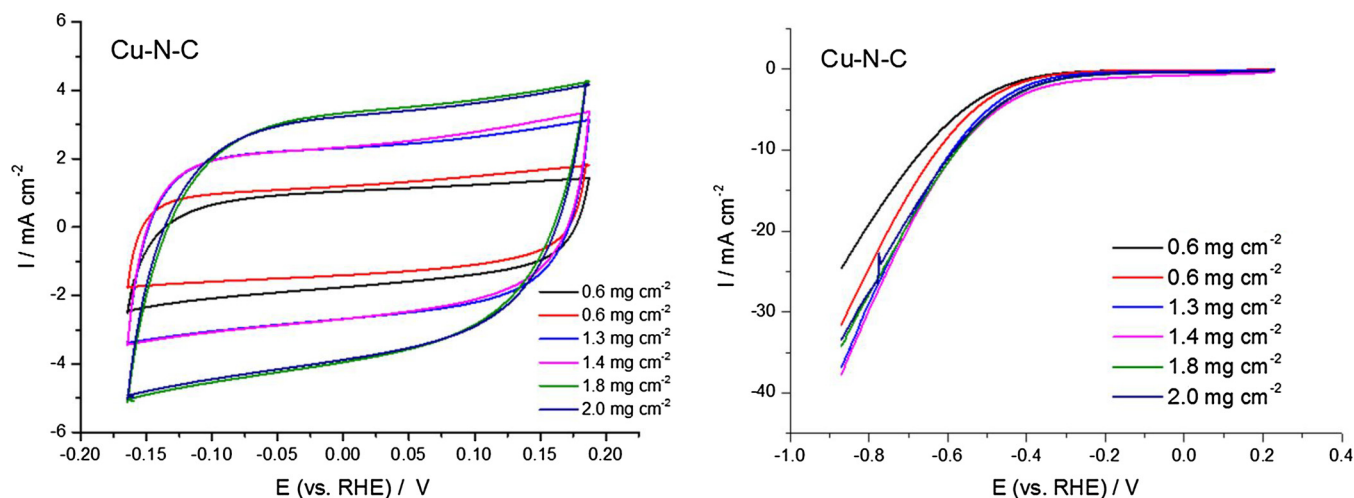**Fig. 4.** XPS data for Cu–N–C (A and B) and Mo–N–C (C) synthesized by SSM.

Fig. 5. CV and LSV curves recorded for the Cu–N–C catalyst with different layer thickness, in 0.5 M KHCO$_3$/CO$_2$ solution at 50 mV s^{-1} sweep rate.

dependent on the type of the metal in the carbon structure.

The reaction products were also analyzed during the potentiostatic electrolysis. No liquid phase product formed (according to GC–MS analysis), so only the analysis of the gas phase is presented in what follows. CO and H$_2$ were detected in all the cases, although with distinctly different ratios. The highest CO/H$_2$ ratio was obtained for the bare C–N sample: approximately 50–50% at moderate bias potentials, which altered to 30% CO$_2$ER and 70% HER at more negative potentials. To verify that the CO is originated from the reduction of CO$_2$ and not from the degradation of the M–N–C catalyst, long-term electrolysis

measurements for the metal-free catalyst were repeated using NaH^{13}CO$_3$ electrolyte saturated with ^{12}CO$_2$. The GC–MS traces corresponding to the molecule ions of ^{12}CO (m/z = 28) and ^{13}CO (m/z = 29) are shown in Fig. 8A and B. While only 1% of the total CO is ^{13}CO when using unlabeled bicarbonate (which corresponds to the natural abundance of ^{13}C), 55% of the total CO is ^{13}CO when the NaH^{13}CO$_3$ electrolyte is used. This value is close to the total ^{13}C amount (60%) in the cell. The amount of ^{29}CO increases continuously with reaction time (Fig. 7B) and the intensity ratios of the m/z = 28 and m/z = 29 signals remain stable during 90 min s of electrolysis in both cases (Fig. 8C and
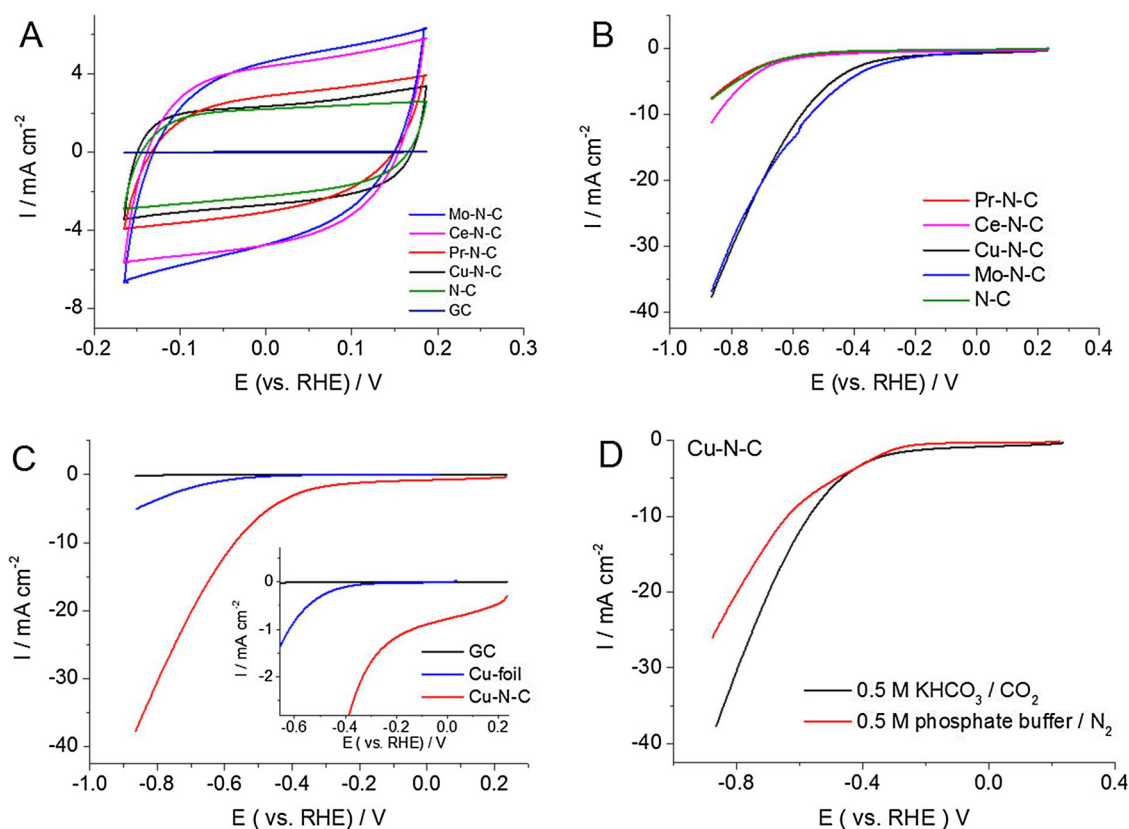

Fig. 6. CVs of the catalyst layers, in a 0.5 M KHCO$_3$ solution saturated with CO$_2$ (pH = 7.4) at 50 mV s^{-1} scan rate (A). Linear sweep voltammograms of the five catalyst layers (B) and the benchmark GC and Cu electrodes (C) in a CO$_2$-saturated 0.5 M KHCO$_3$ (pH = 7.4) solution with 5 mV s^{-1} scan rate. Comparison of the LSV curves of the Cu–N–C catalyst layer in a CO$_2$-saturated (0.5 M KHCO$_3$ / CO$_2$) and a CO$_2$-free electrolyte (0.5 M phosphate buffer). The catalyst loading was 1.5 mg cm^{-2} for all samples.
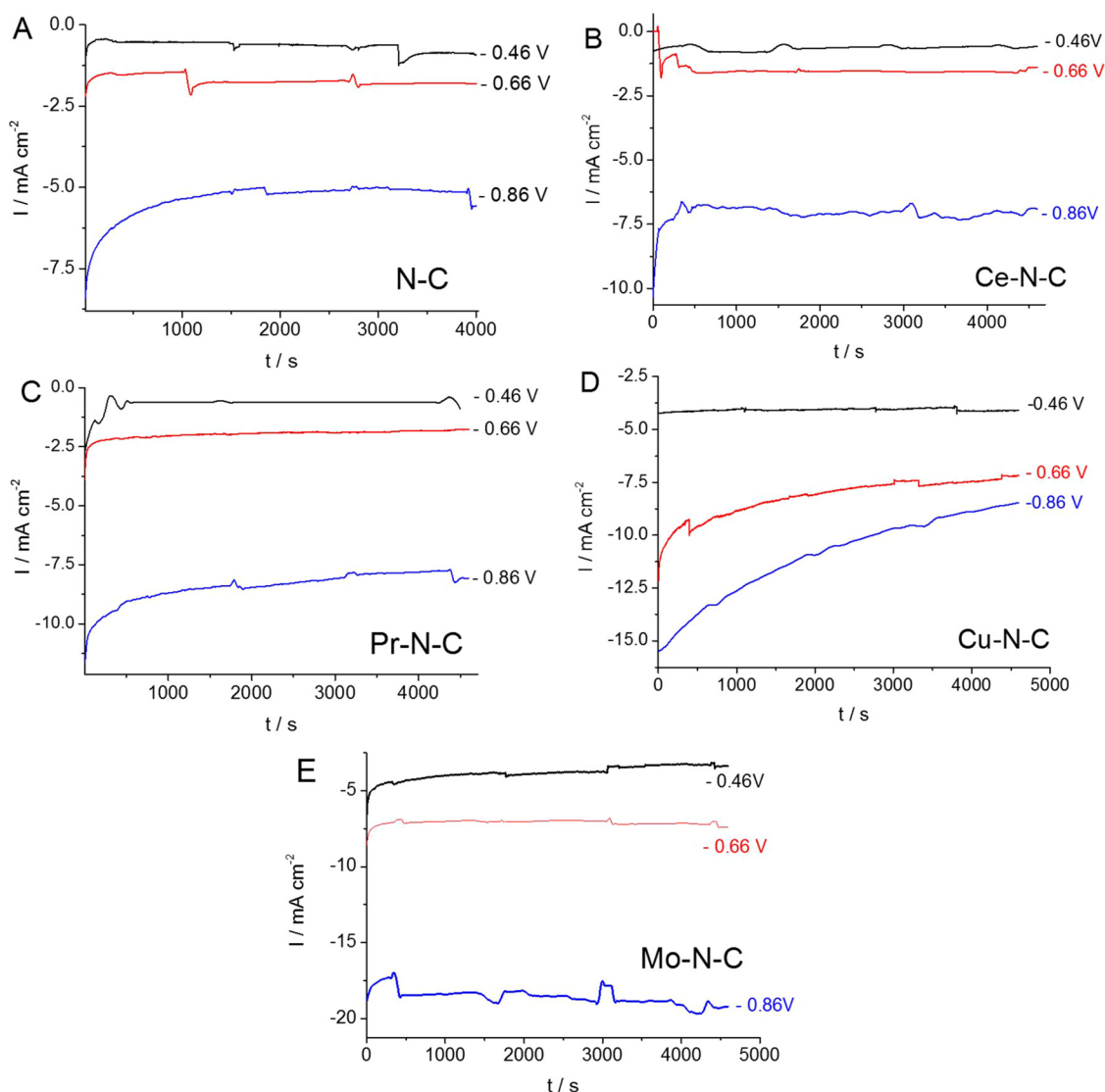
Fig. 7. Chronoamperometric curves recorded during potentiostatic electrolysis in a CO_2-saturated 0.5 M $KHCO_3$ electrolyte for all electrocatalysts at three different potentials.

D).

For the Cu and Mo-containing samples only trace amounts (< 1%) of CO was formed at all the studied potentials, all the rest of the passed charge accounted for H_2-evolution. Note that these were the samples which gave the highest currents. For the Pr and Ce-containing samples, 6 and 14% of the charge was associated to the formation of CO, and all the rest accounted for the HER. These trends are quantitatively shown in Fig. 9B, where the partial current densities for CO_2ER and HER are compared for the different samples at $E = -0.66$ V (vs. RHE) Overall, it seems that the introduction of metal atoms in the structure increases the overall electroactivity, although at different extent for the different metals. This current increase is related to an enhanced HER performance on the Cu and Mo centers. At the same time, CO_2 converting electrocatalytic property seems to be an intrinsic feature of the bare N-doped carbon material, and this activity decreased upon the introduction of metals.

Although four different metal-containing samples were compared with the bare C–N catalyst, and electrolysis was performed at three different potentials in each case, it is very difficult to draw quantitative structure–property correlations. A definite trend was identified between the amount of metals and the HER performance (Fig. 9D), as well as between the amount of pyridinic nitrogen and the electrocatalytic

performance (both CO_2ER and HER). This latter effect, however, was complex: the higher ratio of pyridine-type N-atoms in the catalyst resulted in higher HER performance, but lower CO_2ER activity. Clearly, further systematic studies need to be performed to completely understand the role of different moieties in dictating the electrocatalytic performance of these M–N–C materials. It is also worth noting that in parallel to the increase in the HER activity, there was *always* a decrease in the CO_2ER performance, which suggest that some initially active N–C moieties disappear upon the metal incorporation.

4. Conclusions

The electrocatalytic activity of a set of M–N–C catalysts (M: Cu, Mo, Ce, Pr) towards CO_2ER and HER was studied for the first time. These high surface area electrocatalysts were obtained via a sacrificial support method, using silica nanoparticles as seeds. Electron microscopic methods proved that the catalysts have a highly porous structure, because of the presence of the silica support during the synthesis. The electrochemical response of the Pr–N–C and the N–C was almost identical, while there was a slight current increase below $E = -0.7$ V (vs. RHE) for the Ce-containing sample. In contrast, the Mo- and Cu-containing catalysts showed about 300 mV less negative onset potential
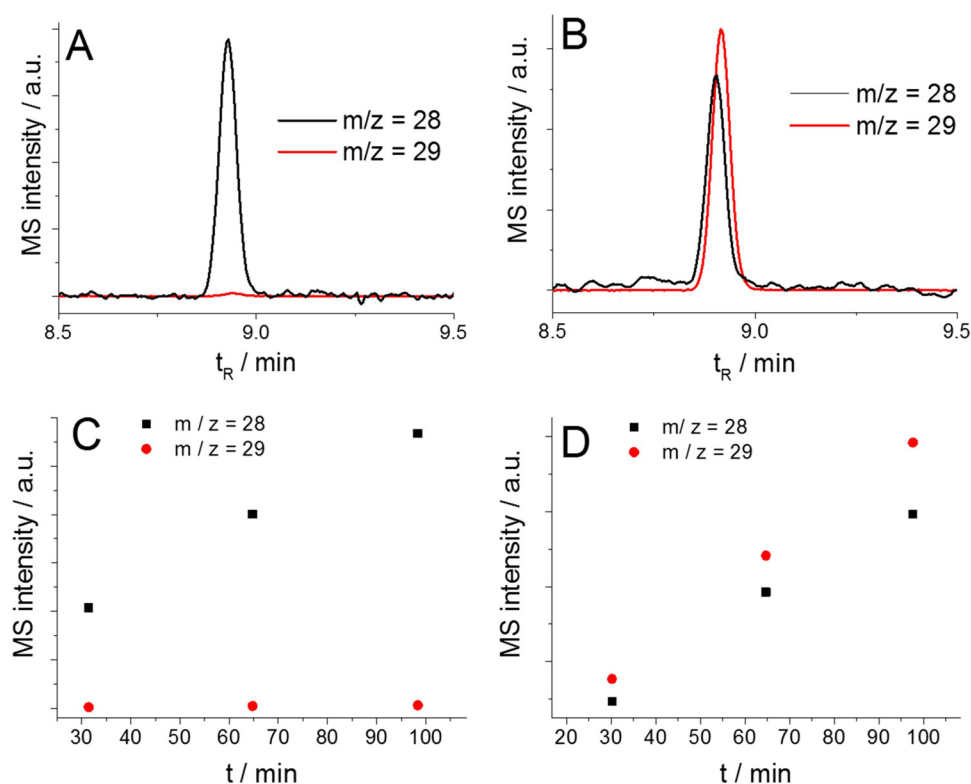
Fig. 8. Chromatograms (recorded in the 30th minute of electrolysis) corresponding to the $m/z = 28$ and $m/z = 29$ molecule ions (captured using selective ion monitoring) of the generated carbon monoxide, using ^{12}C (A) and ^{13}C (B) containing reactants. Intensities of the signals of the $m/z = 28$ and $m/z = 29$ molecule ions with increasing electrolysis time in the experiments using unlabeled (C) and labeled (D) carbon source.

and considerably higher reduction currents, compared to the metal-free catalyst and corresponding metal foil. Notably, the presence of metal precursors during the synthesis, affected the N–C structure as well (as deduced from the relative share of different N-functions). Consequently,

the factors underpinning the changes of the CO_2ER and HER activity in the series of samples are complex and convoluted. Most importantly, the massive enhancement in the HER performance was witnessed for the Cu and Mo-containing samples, where small sized nanoparticles and
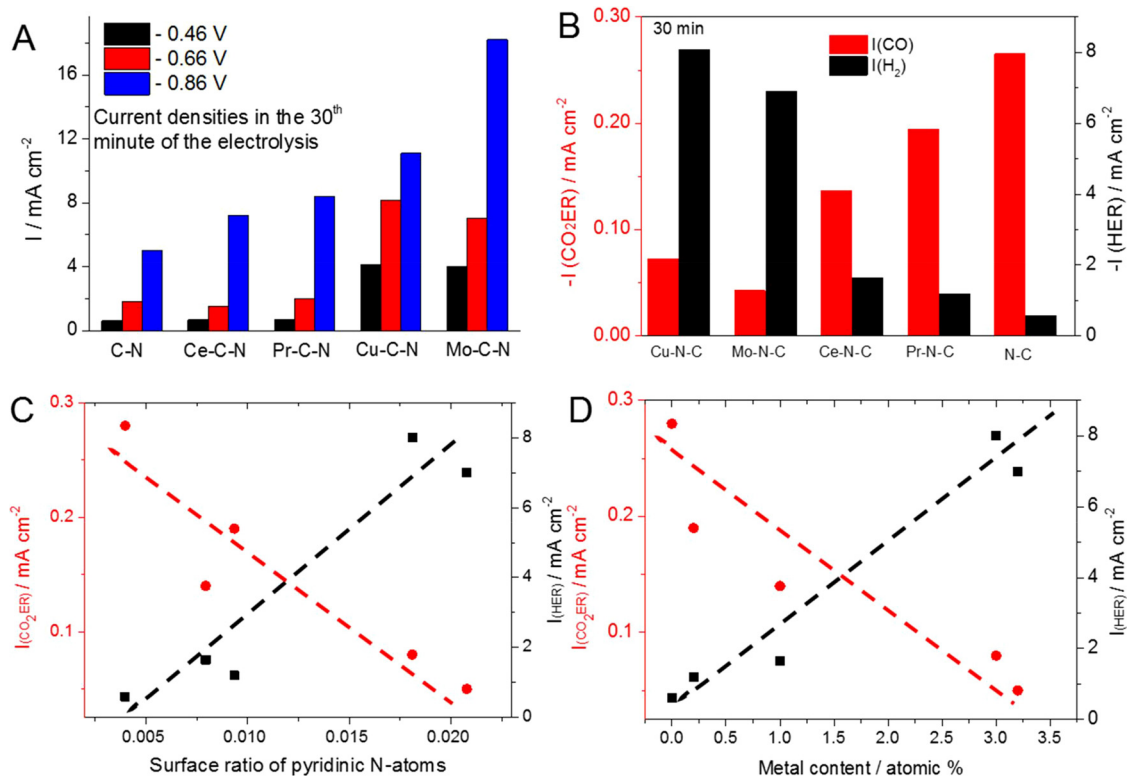

Fig. 9. Total current densities recorded in the 30th minute of the electrolysis for all five catalysts. (A) Partial current densities recorded at $E = -0.66\,V$ (B). Partial current density vs. surface composition plots for all five catalysts, showing the role of pyridinic N-atoms (C) and metal atoms (D). The dashed lines serve only as guides to the eye.

M–N bonds were both detected. ^{13}C isotope labeling studies proved that the formed CO originates from the precursors CO_2/HCO_3^-, and not the carbon-based electrode. At this juncture, it would be premature to identify which component of the synthesized M–N–C catalyst is responsible for the enhanced HER performance, but we are confident that there is considerable scope in synthesizing such metal containing N-doped carbon catalysts in the search for cheap alternatives of noble metals.

Acknowledgements

References

[1] J. Qiao, Y. Liu, F. Hong, J. Zhang, Chem. Soc. Rev. 43 (2014) 631–675.
[2] B. Endrodi, G. Bencsik, F. Darvas, R. Jones, K. Rajeshwar, C. Janáky, Prog. Energy Combust. Sci. 62 (2017) 133–135.
[3] Y. Hori, G.-A.M, C.G. Vayenas, R.E. White, Electrochemical CO_2 reduction on metal electrodes, Mod. Asp. Electrochem. Springer New York, 2008, pp. 89–189.
[4] O.A. Baturina, Q. Lu, M.A. Padilla, L. Xin, W. Li, A. Serov, et al., ACS Catal. 4 (2014) 3682–3695.
[5] R.J. Lim, M. Xie, M.A. Sk, J.-M. Lee, A. Fisher, X. Wang, et al., Catal. Today 233 (2014) 169–180.
[6] A. Dutta, M. Rahaman, N.C. Luedi, M. Mohos, P. Broekmann, ACS Catal. 6 (2016) 3804–3814.
[7] S. Zhao, S. Guo, C. Zhu, J. Gao, H. Li, H. Huang, et al., RSC Adv. 7 (2017) 1376–1381.
[8] J. Lai, S. Li, F. Wu, M. Saqib, R. Luque, G. Xu, Energy Environ. Sci. 9 (2016) 1210–1214.
[9] T. Liu, S. Ali, Z. Lian, B. Li, D.S. Su, J. Mater. Chem. A 5 (2017) 21596–21603.
[10] W. Zhou, J. Jia, J. Lu, L. Yang, D. Hou, G. Li, et al., Nano Energy 28 (2016) 29–43.
[11] Y. Zheng, Y. Jiao, Y. Zhu, L.H. Li, Y. Han, Y. Chen, et al., Nat. Commun. 5 (2014) 1–8.
[12] J. Zhang, L. Qu, G. Shi, J. Liu, J. Chen, L. Dai, Angew. Chem. 128 (2016) 2270–2274.
[13] K. Qu, Y. Zheng, X. Zhang, K. Davey, S. Dai, S.Z. Qiao, ACS Nano 11 (2017) 7293–7300.
[14] J. Wu, R.M. Yadav, M. Liu, P.P. Sharma, C.S. Tiwary, L. Ma, et al., ACS Nano 9 (2015) 5364–5371.
[15] J. Wu, M. Liu, P.P. Sharma, R.M. Yadav, L. Ma, Y. Yang, et al., Nano Lett. 16 (2016) 466–470.
[16] H.-R.M. Jhong, C.E. Tornow, B. Smid, A.A. Gewirth, S.M. Lyth, P.J.A. Kenis, ChemSusChem 10 (2017) 1094–1099.
[17] J. Xu, Y. Kan, R. Huang, B. Zhang, B. Wang, K.H. Wu, et al., ChemSusChem 9 (2016) 1085–1089.
[18] P.P. Sharma, J. Wu, R.M. Yadav, M. Liu, C.J. Wright, C.S. Tiwary, et al., Angew. Chem. Int. Ed. 54 (2015) 13701–13705.
[19] X. Sun, X. Kang, Q. Zhu, J. Ma, G. Yang, Z. Liu, et al., Chem. Sci. 7 (2016) 2883–2887.
[20] J. Wu, S. Ma, J. Sun, J.I. Gold, C. Tiwary, B. Kim, et al., Nat. Commun. 7 (2016) 13869.
[21] W. Li, M. Seredych, E. Rodríguez-Castellón, T.J. Bandosz, ChemSusChem 9 (2016) 606–616.
[22] B. Dembinska, W. Kiciński, A. Januszewska, A. Dobrzeniecka, P.J. Kulesza, J. Electrochem. Soc. 164 (2017) H484–H490.
[23] D. Hursán, C. Janáky, ACS Energy Lett. 3 (2018) 722–723.
[24] S. Wannakao, N. Artrith, J. Limtrakul, A.M. Kolpak, ChemSusChem 8 (2015) 2745–2751.
[25] Z.-L. Wang, C. Li, Y. Yamauchi, Nano Today 11 (2016) 373–391.
[26] T.N. Huan, G. Ranjbar, G. Rousse, M. Sougrati, A. Zitolo, V. Mougel, et al., ACS Catal. 7 (2017) 1520–1525.
[27] L. Fan, P.F. Liu, X. Yan, L. Gu, Z.Z. Yang, H.G. Yang, et al., Nat. Commun. 7 (2016) 10667.
[28] Z.L. Wang, X.F. Hao, Z. Jiang, X.P. Sun, D. Xu, J. Wang, et al., J. Am. Chem. Soc. 137 (2015) 15070–15073.
[29] F. Wang, Y. Sun, Y. He, L. Liu, J. Xu, X. Zhao, et al., Nano Energy 37 (2017) 1–6.
[30] A.S. Varela, N. Ranjbar Sahraie, J. Steinberg, W. Ju, H.-S. Oh, P. Strasser, Angew. Chem. Int. Ed. 54 (2015) 10758–10762.
[31] P. Su, K. Iwase, S. Nakanishi, K. Hashimoto, K. Kamiya, Small 12 (2016) 6083–6089.
[32] X. Li, W. Bi, M. Chen, Y. Sun, H. Ju, W. Yan, et al., J. Am. Chem. Soc. 139 (2017) 14889–14892.
[33] F. Pan, W. Deng, C. Justiniano, Y. Li, Appl. Catal. B Environ. 226 (2018) 463–472.
[34] W. Ju, A. Bagger, G.-P. Hao, A.S. Varela, I. Sinev, V. Bon, et al., Nat. Commun. 8 (2017) 944.
[35] K. Jiang, S. Siahrostami, T. Zheng, Y. Hu, S. Hwang, E. Stavitski, et al., Energy Environ. Sci. (2018), http://dx.doi.org/10.1039/C7EE03245E.
[36] C. Zhao, X. Dai, T. Yao, W. Chen, X. Wang, J. Wang, et al., J. Am. Chem. Soc. 139 (2017) 8078–8081.
[37] A. Serov, M. Padilla, A.J. Roy, P. Atanassov, T. Sakamoto, K. Asazawa, et al., Angew. Chem. Int. Ed. 53 (2014) 10336–10339.
[38] U. Martinez, A. Serov, M. Padilla, P. Atanassov, ChemSusChem 7 (2014) 2351–2357.
[39] A. Serov, N.I. Andersen, A.J. Roy, I. Matanovic, K. Artyushkova, P. Atanassov, J. Electrochem. Soc. 162 (2015) F449–F454.
[40] D. Sebastián, V. Baglio, A.S. Aricò, A. Serov, P. Atanassov, Appl. Catal. B Environ. 182 (2016) 297–305.
[41] C. Janáky, D. Hursan, B. Endrődi, W. Chanmanee, D. Roy, D. Liu, et al., ACS Energy Lett. 1 (2016) 332–338.
[42] M.J. Workman, M. Dzara, C. Ngo, S. Pylypenko, A. Serov, S. McKinney, et al., J. Power Sources 348 (2017) 30–39.
[43] D. Sebastián, A. Serov, K. Artyushkova, P. Atanassov, A.S. Aricò, V. Baglio, J. Power Sources 319 (2016) 235–246.
[44] C. Santoro, A. Serov, C.W. Narvaez Villarrubia, S. Stariha, S. Babanova, K. Artyushkova, et al., Sci. Rep. 5 (2015) 16596.
[45] N.D. Leonard, K. Artyushkova, B. Halevi, A. Serov, P. Atanassov, S.C. Barton, 162 (2015) F1253–F1261.
[46] K. Artyushkova, A. Serov, S. Rojas-Carbonell, P. Atanassov, J. Phys. Chem. C 119 (2015) 25917–25928.